

Largely Improved Near-Infrared Silicon-Photosensing by the Piezo-Phototronic Effect

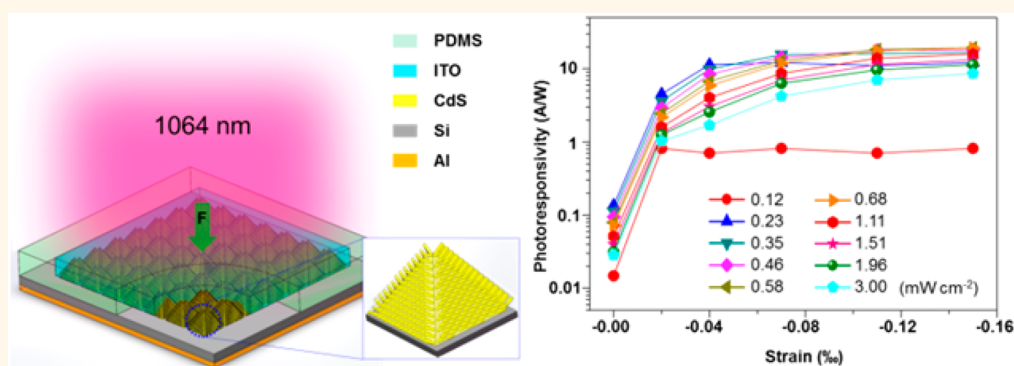
Yejing Dai,^{†,‡,⊥} Xingfu Wang,^{†,⊥} Wenbo Peng,^{†,⊥} Haiyang Zou,[†] Ruomeng Yu,[†] Yong Ding,[†] Changsheng Wu,[†] and Zhong Lin Wang^{*,†,§,⊥}

[†]School of Materials Science and Engineering, Georgia Institute of Technology, Atlanta, Georgia 30332-0245, United States

[‡]Key Laboratory of Advanced Ceramics and Machining Technology, Ministry of Education, School of Materials Science and Engineering, Tianjin University, Tianjin 300072, China

[§]Beijing Institute of Nanoenergy and Nanosystems, Chinese Academy of Sciences, Beijing 100083, China

Supporting Information



ABSTRACT: Although silicon (Si) devices are the backbone of modern (opto-)electronics, infrared Si-photosensing suffers from low-efficiency due to its limitation in light-absorption. Here, we demonstrate a large improvement in the performance, equivalent to a 366-fold enhancement in photoresponsivity, of a Si-based near-infrared (NIR) photodetector (PD) by introducing the piezo-phototronic effect via a deposited CdS layer. By externally applying a -0.15% compressive strain to the heterojunction, carrier-dynamics modulation at the local junction can be induced by the piezoelectric polarization, and the photoresponsivity and detectivity of the PD exhibit an enhancement of two orders of magnitude, with the peak values up to 19.4 A/W and 1.8×10^{12} cm Hz^{1/2}/W, respectively. The obtained maximum responsivity is considerably larger than those of commercial Si and InGaAs PDs in the NIR waveband. Meanwhile, the rise time and fall time are reduced by 84.6% and 76.1% under the external compressive strain. This work provides a cost-effective approach to achieve high-performance NIR photosensing by the piezo-phototronic effect for high-integration Si-based optoelectronic systems.

KEYWORDS: near-infrared, Si-based, CdS nanowire, photosensing, piezo-phototronic effect

Near-infrared (NIR) wavelength sensing has attracted tremendous attention owing to its broad applications in biological imaging, communications, environmental monitoring, medical treatment, spectroscopy, security, etc.^{1–6} In the past few decades, numerous NIR photodetectors (PDs) with favorable photoresponse performances were demonstrated based on single-crystalline InGaAs,⁷ PbS quantum-dots,⁸ two-dimensional layered materials,⁹ organic semiconductors,¹⁰ photomultiplier tubes,¹¹ etc. Most of them possess drawbacks such as extreme cost, complex fabrication, and strict operation environment. In addition, simultaneously optimizing photoresponsivity and response speed remains as a challenge to further expand the practical applications of NIR PDs.¹²

Silicon (Si), as one of the most important substrates for optoelectronic applications, is of particular interest for PD applications by integrating with other semiconductors.^{13,14} Si-based PDs can be well operated at the harsh environment with broadband and good compatibility,¹⁵ making them an attractive alternative for NIR detection. Although the absorption wavelength of Si covers wide spectral range from ultraviolet (UV) to NIR, most of existing Si-based PDs are limited in the visible spectrum range (below the wavelength of ~ 800 nm) due to the rapidly declined photoresponsivity caused by low photon

Received: April 23, 2017

Accepted: July 10, 2017

Published: July 10, 2017



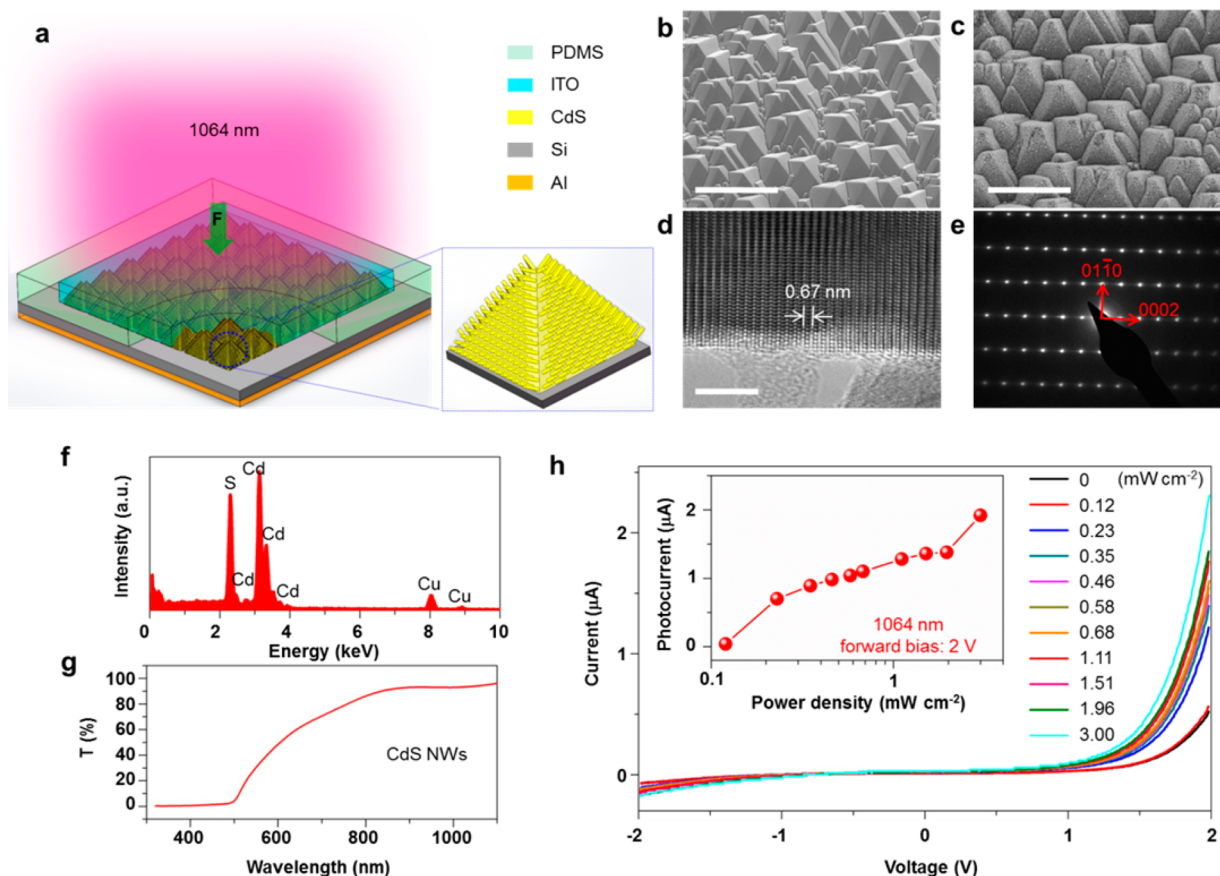


Figure 1. Device structure, characterization and property. (a) Schematic structure of a p-Si/n-CdS NWs heterostructure NIR PD. (b, c) SEM images of (b) the etched Si wafer and (c) the CdS NW array synthesized on the etched Si wafer. The scale bar is 20 μm. (d) High resolution transmission electron microscopy (HRTEM) image and (e) corresponding select area electron diffraction (SAED) pattern of a CdS NW. The scale bar in panel d is 5 nm. (f) Energy dispersive X-ray (EDX) spectrum of single CdS NW. (g) Transmission spectrum of CdS NW array grown on the FTO/glass substrate. (h) *I*–*V* characteristics of the device under different illumination power densities when a 2 V bias is applied. The inset shows the photocurrent changes with the power density at 2 V forward bias.

excitation energy and relatively weak light absorption in NIR waveband.^{8,10,15,16} Therefore, it is of great significance to explore a simple and cost-saving approach for high-performance Si-based NIR PDs with improved photoresponsivity.

Generally, the generation and separation efficiency as well as the transport behaviors of the photogenerated carriers are important to the photoresponse performances of PDs. In piezoelectric semiconductor materials (ZnO, CdS, GaN, *etc.*), the mechanical strain-induced piezoelectric polarization charges¹⁷ (piezo-charges) at the local interface can effectively tune/control the optoelectronic processes of the charge carriers, such as generation, separation, transport, and recombination, which is referred to the piezo-phototronic effect.¹⁸ This emerging effect has drawn increasing research interest and led to enhanced device characteristics and numerous applications in various fields such as PDs,^{19–21} solar cells,^{22,23} light emission diodes,^{24–26} and many more.^{27,28}

In this work, a p-silicon/n-CdS nanowires (NWs) heterostructure NIR PD is fabricated by hydrothermally synthesizing the piezoelectric semiconductor nanomaterial, CdS NWs, on the textured-Si substrate. By introducing the piezo-phototronic effect, the photoresponsivity, specific detectivity, and response speed of the Si-based NIR PD are drastically improved. Under a forward bias of 2 V, the photoresponsivity *R* increases from 79.7 mA/W to 19.4 A/W when a –0.15% externally static compressive strain is applied, and its value could be enhanced

by ~366-times. The detectivity *D*^{*} is improved by two orders of magnitude with its peak value up to 1.8×10^{12} Jones (cm Hz^{1/2}/W). Furthermore, both rise time and fall time decrease from 63 to 9.7 ms and from 36 to 8.6 ms, respectively. The corresponding physical mechanisms are systematically analyzed and revealed by theoretically calculating the depletion region dynamics and energy band profiles of the Si-based pn junction PD under different strain conditions via finite element analysis (FEA). This work not only presents an in-depth understanding of the fundamental piezo-phototronic effect in pn heterostructures, but also provides a cost-effective and unconventional path to develop high-performance Si-based NIR photosensing.

RESULTS AND DISCUSSION

Device Performances. The device structure of the p-Si/n-CdS NWs heterostructure NIR PD is schematically shown in Figure 1a. To increase the effective surface area and enhance the light absorption efficiency, a surface-textured p-Si substrate, covered by micropylramids with a bottom edge length of 3–7 μm (Figure 1b), was produced by wet chemical etching. High-density CdS NW array was then directly grown perpendicular to the surface of Si micropylramids via one-step hydrothermal synthesis (Figure 1c), forming a pn junction between the p-Si substrate and –c end of CdS NWs. The diameter and length of the NWs, on average, are 50 and 600 nm, respectively. Detailed device fabrication of our Si-based pn junction NIR PD is

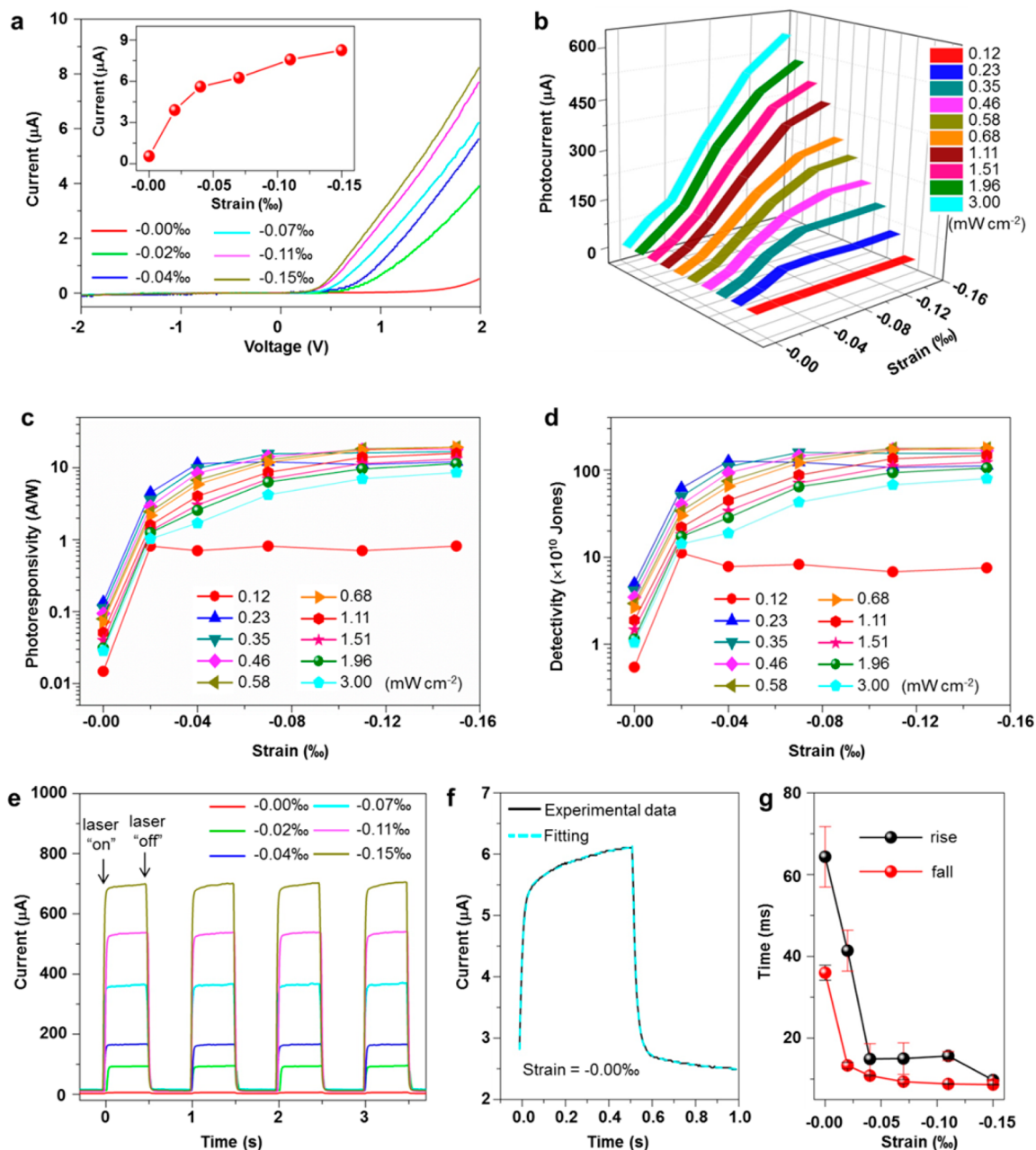


Figure 2. Piezo-phototronic effect on the p-Si/n-CdS NWs heterostructure NIR PD. (a) I - V characteristics of the device under different strains without laser illumination. The inset shows the output current changes with the external compressive strain at 2 V forward bias. (b) Photocurrent, (c) photoresponsivity, and (d) detectivity of the device under different strains and illumination conditions when the forward bias is 2 V. (e) Time response and repeatability of the device for different strains under 1064 nm illumination at a power density of 3 mW cm^{-2} . (f) Enlarged time response and recovery curve of one cycle under -0.00% external strain and the fitted curve using the second-order exponential decay function. (g) Corresponding rise time and fall time of the device under different compressive strains.

illustrated in the [Methods](#). Single-crystalline wurtzite structure and polar c -axis growth direction of the as-grown CdS NWs were confirmed by high-resolution transmission electron microscopy (HRTEM) image ([Figure 1d](#)) and corresponding select area electron diffraction (SAED) pattern ([Figure 1e](#)). The energy dispersive X-ray (EDX) spectrum ([Figure 1f](#)) also verifies the successful growth of CdS NWs.

To investigate the photoresponse performances of the p-Si/n-CdS NWs NIR PD, transmission property of CdS NWs, grown on a FTO/glass substrate under the same conditions as those on the etched Si substrate, was characterized and presented in [Figure 1g](#). It is clear that the as-synthesized CdS

NWs exhibit superior transmission and little absorption in the NIR waveband (e.g., $T > 95\%$ for 1064 nm), indicating that the photogenerated carriers are mainly from the p-Si side at the local junction/interface when the device is under 1064 nm NIR illumination. [Figure S1](#) in the [Supporting Information](#) shows the photoresponsivity and photocurrent of p-Si/n-CdS NWs heterostructure PD for 325, 442, 650, 808, and 1064 nm wavelengths under +2 V forward bias, showing a broad spectral response from UV to NIR. Photoresponsivity was defined as $R = \frac{\Delta I}{P_{\text{ill}}}$, where $P_{\text{ill}} = I_{\text{ill}} \times A$ is the illumination power on the PD, I_{ill} is the power density, A is the effective area of the PD,

and $\Delta I = I_{\text{light}} - I_{\text{dark}}$ (I_{light} and I_{dark} are the output currents with and without laser illumination).^{10,20} A maximum photoresponsivity (R) has been found to be 59.3 mA/W at around 808 nm wavelength. The current–voltage (I – V) characteristics of the NIR PD illuminated under a series of laser power densities (1064 nm) are shown in Figure 1h, with the relationship between photocurrent and power density under a 2 V forward bias plotted in the inset. The strong rectification behavior and low reverse leakage current imply the high quality of the pn junction between p-Si and n-CdS. Furthermore, the photocurrent of the pn junction NIR PD increases step by step with the laser power density. In the incident power density range, the linearity of the photoresponse is good ($r^2 \approx 0.92$).

The piezo-phototronic effect on the photoresponse performances of our NIR PD was explored by applying different static compressive strains under 1064 nm laser illumination, with results summarized in Figure 2. Details about the application and calculation of the externally applied compressive strains are illustrated in Supporting Information (Section E). I – V characteristics of the device under a series of compressive strains ranging from -0.00% to -0.15% without laser illumination were measured and plotted in Figure 2a. At a certain fixed forward bias, the device output current was obviously increased as the externally applied static compressive strain increased (insert in Figure 2a). Meanwhile, the calculated rectification ratio of the pn junction increased greatly from 7.3 to 115, and the turn-on voltage decreased from 1.5 to 0.3 V. These are attributed to the enhanced separation efficiency of the charge carriers and improved rectifying behavior in the pn junction NIR PD caused by the externally applied compressive strain. A 1064 nm laser with ten different power densities (varying between 0.12 and 3.00 mW cm⁻²) was then introduced and shined onto the NIR PD. The device output currents under each power density and each external strain at the bias of +2 V were collected and summarized in Figure S2a, indicating that the output current can be increased by increasing either the external strain or the laser power density. The corresponding photocurrents ΔI are calculated at each strain condition and presented in Figure 2b. Under a certain power density of illumination, ΔI exhibits a substantial increase as the external strain increasing from -0.00% to -0.15% , indicating the significant performance enhancement of the NIR PD by the piezo-phototronic effect.

Critical parameters of PDs, the photoresponsivity R , and specific detectivity D^* are further calculated for all power densities and external strains with the 2 V forward bias (Figure 2c,d). D^* is defined as $D^* = \frac{R}{\sqrt{2qJ_d}}$, where q is the electronic charge, and J_d is the dark current density.^{10,29} Generally, the R and D^* gradually increase with external strain and reach saturation when the strain reaches a certain value. For example, when the strain is more than -0.04% , the values of R and D^* for 0.23 mW cm⁻² power density almost keep unchanged with the further increase in strain. This may be due to the limited number of photons generated under relative weak power density, and thus, the enhanced generation, separation and transport of photogenerated carriers derived from the applied compressive strain would reach saturation at a certain strain value. However, for strong power densities more than 0.46 mW cm⁻², the values of R and D^* gradually increase and finally reach maximum values under -0.15% compressive strain due to the sufficient number of photons. More than two orders of magnitude enhancement in R and D^* was observed compared

to those at the same power density condition but under the strain-free condition. The relative changes of R as $\Delta R/R_0$ ($\Delta R = R_s - R_0$, R_s is the R under a certain strain, and R_0 is the R value under strain-free condition) for each power density are further calculated to better illustrate the piezo-phototronic effect on the R value (Figure S2b). The calculated $\Delta R/R_0$ drastically increases with the externally applied compressive strain. Up to a 366-fold enhancement of $\Delta R/R_0$ was achieved by applying -0.15% compressive strain when power density was fixed at 1.96 mW cm⁻². Furthermore, under a power density of 0.58 mW cm⁻², the largest R and D^* were calculated to be 19.4 A/W and 1.8×10^{12} Jones, respectively. This maximum R value is significantly larger than that of commercial Si photodiodes (0.1–0.3 A/W at 1100 nm) and commercial InGaAs photodiodes (0.6–0.8 A/W at 1100 nm)^{30,31} and is also dozens to thousands of times larger than that of previously reported NIR PDs based on Si/semiconductor heterostructures.^{32–34} Moreover, p-Si/n-ZnO NWs heterostructure NIR PDs were also fabricated by hydrothermally synthesizing ZnO NW array instead of CdS NW array on the textured p-Si substrate (Section B in Supporting Information). Similar photoresponse measurements were conducted to certify the piezo-phototronic effect on the performance of the p-Si/n-ZnO NIR PDs, and corresponding results are shown in Figure S3. By introducing the piezo-phototronic effect, the R and D^* values are also improved. Under a forward bias of 0.5 V, the R increases from 12.4 mA/W to 7.4 A/W for 0.36 mW cm⁻² power density when a -0.10% externally compressive strain is applied, and the maximum $\Delta R/R_0$ is 782 for 0.18 mW cm⁻² power density. The detectivity D^* is also improved by two orders of magnitude with its peak value up to 6.0×10^{11} Jones. Obviously, with the increase of externally applied compressive strain from -0.00% to -0.10% , corresponding R and D^* of p-Si/n-ZnO NIR PDs exhibit the same trends and approximate magnitude of enhancement.

Under a forward bias of 2 V, response speed and repeatability of a typical p-Si/n-CdS NWs NIR PD were tested under various external strain conditions by switching the 1064 nm laser with a fixed power density of 3.00 mW cm⁻² (Figure 2e). The output current presents impressive consistency and repeatability for all external strain conditions. Corresponding weight-averaged rise time and fall time of the PD are calculated from the I – t curve under each strain condition based on the best fit second-order exponential decay function.^{20,35} As shown in Figure 2f, a typical single cycle of the acquired I – t data under the strain-free condition can be perfectly fitted by the corresponding fitting curve. The rise time and fall times of the p-Si/n-CdS NWs NIR PD as a function of the externally applied compressive strain were extracted and summarized in Figure 2g. As the external strain increases from -0.00% to -0.15% , the rise time markedly decreases from 63 to 9.7 ms, and fall time decreases from 36 to 8.6 ms, which correspond to an 84.6% and 76.1% reduction, respectively. The significant improvement in photoresponsivity, detectivity, and response speed of our Si-based NIR PD indicates that the compressive-strain-induced positive piezo-charges located at the $-c$ end of CdS NWs largely enhance the separation and transport behavior of photogenerated carriers.

Confirmation of the Piezo-Phototronic Effect. To verify that the performance enhancement in the Si-based NIR PDs is dominated by the polar piezoelectric potential (piezo-potential) effect, another device configuration was explored by constructing a Si-ZnO pn junction at the $+c$ end of ZnO NWs (Figure

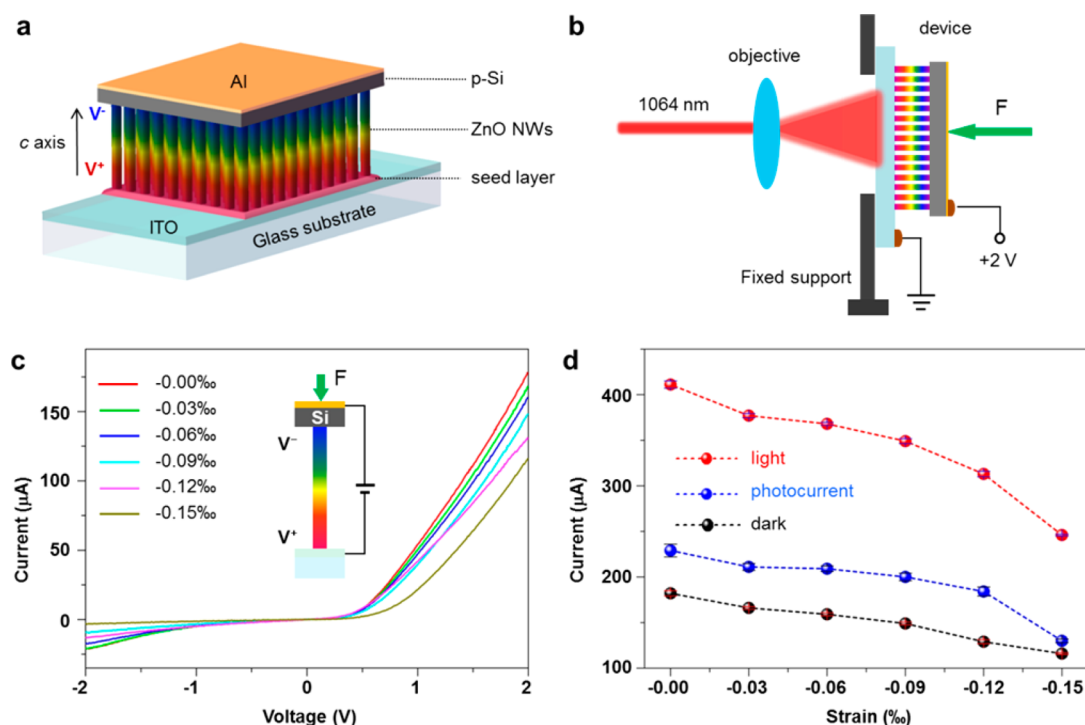


Figure 3. Confirmation of the piezo-phototronic effect. (a) Schematic structure of a p-Si/n-ZnO NWs heterostructure device. (b) Schematic diagram of experimental setup for the p-Si/n-ZnO NWs heterostructure device measurement. (c) I – V characteristics of the p-Si/n-ZnO NWs heterostructure device under different external compressive strains without illumination when a 2 V bias is applied. (d) Light, dark, and photo currents change under different compressive strains when applying a 2 V forward bias.

3a,b and Section C in the Supporting Information). High uniform n-ZnO NW arrays were grown on a ITO/glass substrate and then covered by a piece of p-Si wafer with smooth surface (Figures 3a and S4) to form a tight contacting and stable pn junction. The modulation of the piezo-phototronic effect on the performances of this device was studied using a home-built experimental setup, as schematically shown in Figure 3b. I – V characteristics of the n-ZnO/p-Si NIR PD as a function of externally applied compressive strain without and with 1064 nm laser illumination (3.00 mW cm^{-2}) are presented in Figures 3c and S5, respectively, indicating that the output current gradually decreases with increasing external strain. Under each external strain condition, the output currents under illumination I_{light} under dark condition I_{dark} , and corresponding photocurrent $\Delta I = I_{\text{light}} - I_{\text{dark}}$ are extracted and plotted in Figure 3d. Obviously, the photoresponse performances of the n-ZnO NWs/p-Si NIR PD gradually decline with the increase of external compressive strain, indicating that the negative piezo-charges created at the +c end of ZnO NW exhibit a negative impact on the separation and transport properties of the photogenerated carriers.

To further confirm our experimental results presented above and fully understand the physical mechanisms, nonpiezoelectric n-TiO₂ NWs were grown on the textured p-Si substrate to replace piezoelectric CdS or ZnO NWs, and then a p-Si/n-TiO₂ NWs NIR PD was fabricated (Section D in the Supporting Information). I – V curves of the p-Si/n-TiO₂ NWs heterostructure PD with and without 1064 nm illumination under a 3 V forward bias are shown in Figure S8a. No obvious change was observed in the output currents of the p-Si/n-TiO₂ NWs NIR PD under dark and 1064 nm laser illumination condition (Figure S8b) when the externally applied compressive strain continuously increases from -0.00% to -0.10% . This deeply

and strongly indicates that the performance improvement of our Si-based NIR PDs can be attributed to the piezo-phototronic effect and successfully rules out other nonpolar effects, such as the change of contact, the reflection/refraction of the incident light and/or the piezoresistance.

Working Mechanism. Energy band diagrams of the p-Si/n-CdS heterostructure under various strain conditions are carefully analyzed to illustrate the physical mechanisms of the piezo-phototronic effect on the performances of the NIR PDs. The effects of external compressive strain on the energy band profiles for this pn junction at 0 V and +2 V forward biased condition are presented in Figure 4a and b, respectively. Under the 0 V biased condition (Figure 4a), without external strain (black dotted line), an initial depletion region (gray-filled rectangle) is formed at the local interface of p-Si and n-CdS, along with a conduction band offset $\Delta E_c = 0.35 \text{ eV}$ and a valence band offset $\Delta E_v = 1.65 \text{ eV}$ at this interface according to Anderson's model.³⁶ Once the compressive strain is applied, the positive piezo-charges are created at the end of CdS NWs closed to the pn junction interface and the negative piezo-charges at the other end (upper panel in Figure 4a). Certain amounts of free electrons within n-CdS are attracted by the strain-induced positive piezo-charges, while the free holes within p-Si near the depletion region are repelled toward p-type bulk region, giving rise to the shifted depletion region (blue-filled rectangle) at the pn junction and a significant expansion of the p-type depletion region at the p-Si side (blue line, lower panel in Figure 4a). Therefore, the photon-absorption volume of NIR waveband is effectively increased and more non-equilibrium electron–hole pairs are generated under NIR illumination, considering that the photoinduced carriers are mainly generated at the p-Si side. Furthermore, the effective voltage drop in the p-type depletion region under externally

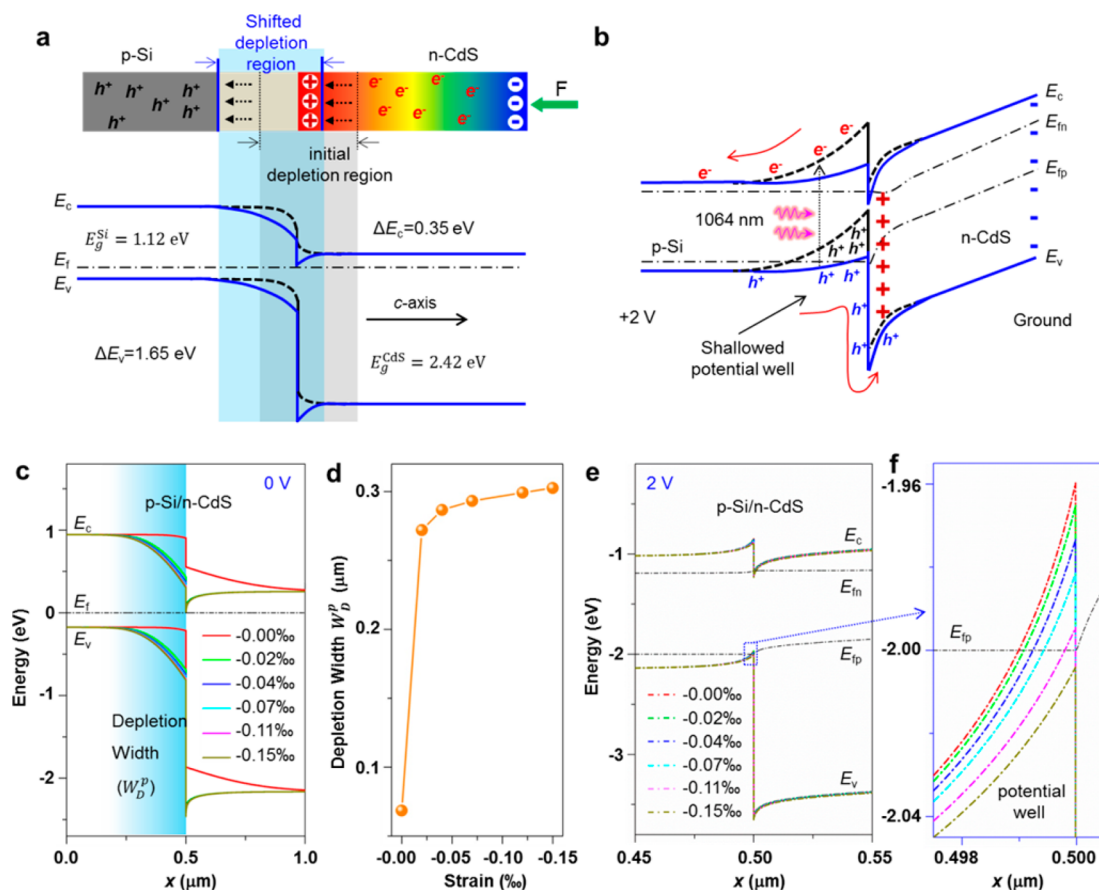


Figure 4. Proposed mechanism and theoretical confirmation for enhanced NIR photoresponse of the p-Si/n-CdS NWs heterostructure NIR PD by the piezo-phototronic effect. (a, b) Schematic band diagrams of a p-Si/n-CdS pn junction without (black dotted line) and with (blue line) a compressive strain (a) under 0 V forward bias and (b) under 2 V forward bias. (c) Calculated band diagrams of the p-Si/n-CdS heterostructure via FEA method for different compressive strains under 0 V forward bias. (d) Dependence of the depletion width (W_D^p) at the p-Si side on applied compressive strain. (e) Calculated band diagrams of the p-Si/n-CdS heterostructure via FEA method for different compressive strains under 2 V forward bias. (f) Enlarged view taken from the marked areas in panel e.

applied forward bias serves as a driving force for the photogenerated carriers and enhances the separation of electron–hole pairs, thus improving the photoresponse and response speed of the NIR PD.

At the +2 V forward biased condition (Figure 4b), the energy band of the pn junction without external compressive straining (black dotted line) indicates that a potential well is naturally formed at the p-Si side near the local junction interface. A large amount of photogenerated holes are confined in this potential well when passing through the junction region; thus, the transport and collection of holes toward the cathode are largely restricted. The photoresponse performance of the NIR PDs is largely limited by the potential-well-induced hole confinement, although the photogenerated electrons can be easily driven toward and collected by the anode. Once the external compressive strain is applied, the energy band in p-type depletion region is lowered (blue line) by the strain-induced positive piezo-charges. Thus, the hole potential well becomes “shallower” compared to that of the strain-free condition, and the corresponding hole confinement is effectively weakened. This leads to the increased hole current and thus the improved photoresponse performance of the pn junction NIR PDs as well as its response speed.

To confirm the physical mechanisms proposed above, theoretical calculations via FEA method were systematically conducted based on the p-Si/n-CdS heterostructure device.

Detailed information about the calculations is found in the Supporting Information (Sections E–G). Under the -0.15% compressive strain, the two dimension (2D) cross-section view and 3D overall view of the piezo-potential distribution in a single Si pyramid are calculated and presented in Figures S9a and S10. The piezo-potential values along the purple line in Figure S9a are extracted and plotted in Figure S9b, indicating that the positive piezo-charges are induced by the externally applied compressive strain and presented at the local interface of the pn junction. It is worth noting that, while a vertical compressive force is applied on the device, the CdS NWs experience shearing force because the applied force is not parallel to the CdS NWs’ growth axis (*i.e.*, the *c*-axis) due to the surface with pyramids. The deformation and strain delivery of the CdS NWs under vertical compressive force in the simulation results are shown in Figure S11 (in Supporting Information). Obviously, the vertical force applied to the CdS NWs can be split into two forces, one along the *a*-axis of the CdS NW and the other along the *c*-axis of the CdS NW as shown in Figure S12. The force along *c*-axis of CdS NW dominantly contributes to the piezo-potential of the bottom surface and the pure piezo-potential of the whole bottom surface of the CdS NWs is positive, which is discussed in detail in Supporting Information (Section F). In addition, the calculated energy band diagrams of the p-Si/n-CdS heterostructure under a series of compressive strain condition without

voltage bias are shown in Figure 4c. By locating the bending point of the energy band, the depletion width (W_{D}) at the p-Si side under each strain condition is determined and plotted in Figure 4d, suggesting that the p-type depletion region significantly increases with the external compressive strain. In the calculated energy diagrams under various external strain conditions at the forward bias of +2 V (Figure 4e,f), the energy band in the p-Si side near the pn junction interface is lowered down, while the depth and volume of the hole potential well in the valence band decrease gradually as the external compressive strain increases. These simulation results completely agree with and further confirm the proposed physical mechanisms in Figure 4a and b.

CONCLUSIONS

In conclusion, we designed and investigated a p-Si/n-CdS NWs heterostructure NIR PD that presents significant enhancement in photoresponse behavior. Photoresponsivity has been improved by 366-fold, which is about two orders of magnitude higher than that of commercial Si PDs in the NIR range, while detectivity and response speed are greatly improved as well. The improvement can be attributed to the piezo-phototronic effect, which greatly helps the separation and transport behavior of photogenerated carriers in the interface/junction. Our low-cost, solution processable and complementary metal–oxide–semiconductor (CMOS)-compatible approach may lead to further explorations in high-performance Si-based PDs, and the promising application of the piezo-phototronic effect to improve the photoresponse performance of other piezo-semiconductor-based optoelectronic devices can also be expected.

METHODS

Device Fabrication Process. First, the p-type (100) silicon wafer (B-doped, 1–10 Ω cm, Universal Wafer) was etched by 5 wt % KOH with 5 vol % isopropanol at 85 $^{\circ}\text{C}$ for 40 min.³⁷ After that, the etched Si wafer with micropylramids was ultrasonically cleaned in acetone, distilled water, and isopropanol for 2 min, respectively. Next, the etched Si wafer was placed into a 100 mL autoclave with the growth surface facing down, and then a mixture solution of 15 mM cadmium nitrate, 15 mM thiourea, and 9 mM glutathione was added to the autoclave. The autoclave was placed into an oven at 200 $^{\circ}\text{C}$ for 8 h for CdS growth,³⁸ and the obtained sample was cleaned with deionized water and dried at 60 $^{\circ}\text{C}$. Subsequently, a top electrode (ITO) and bottom electrode (Al) were deposited by RF magnetron sputtering (PVD75 system, Kurt. J. Lesker Co.) at room temperature, respectively. Finally, a layer of polydimethylsiloxane (PDMS) was spin-coated onto the top electrode to package the device.

Characterization and Measurement. Detailed microscopic structures of the micropylramid structure of Si, CdS NWs, ZnO NWs, and TiO₂ NWs were characterized by SEM (Hitachi SU8010), transmission electron microscopy (TEM) (Tecnai G2) with SAED, and HRTEM (FEI F30) with EDX. Transmission spectra of CdS and TiO₂ NWs were characterized using a UV–visible spectrophotometer (JASCO V-630). *I*–*V* characteristics measurements of the PDs were performed by using a computer-controlled measurement system with a Stanford SRS low noise current preamplifier (SR570)/SRS low noise voltage preamplifier (SR560) in conjunction with a GPIB controller (GPIB-USB-HS, NI 488.2). The optical input stimuli were provided by a He–Cd laser (Model No. K15751I-G, Kimmon Koha Co., Ltd.) and a multichannel fiber coupled laser source (MCLS1, Thorlabs Inc.) whose light power density can be adjusted directly and measured by a thermopile powermeter (Newport 818P-001–12).

ASSOCIATED CONTENT

Supporting Information

The Supporting Information is available free of charge on the ACS Publications website at DOI: 10.1021/acsnano.7b02811.

Performance enhancement in p-Si/n-CdS NWs heterostructure; fabrication and piezo-phototronic effect in p-Si/n-ZnO NWs heterostructure; fabrication of p-Si/n-TiO₂ NWs heterostructure device and transmission spectrum of TiO₂ NWs; calculation of strains applied on CdS NWs and piezo-potential distribution in p-Si/n-CdS heterostructure; discussion of force applied to CdS NWs and its effect on the piezoelectric potential located at the p-Si/n-CdS interface; calculation of external-strain-induced influence on energy band diagrams for p-Si/n-CdS heterojunction (PDF)

AUTHOR INFORMATION

Corresponding Author

*E-mail: zhong.wang@mse.gatech.edu.

ORCID

Zhong Lin Wang: 0000-0002-5530-0380

Author Contributions

[†]These authors contributed equally to this work.

Notes

The authors declare no competing financial interest.

ACKNOWLEDGMENTS

Research was supported by the U.S. Department of Energy, Office of Basic Energy Sciences (Award No. DE-FG02-07ER46394), the National Science Foundation (DMR-1505319), and the “thousands talents” program for pioneer researcher and his innovation team, China, National Natural Science Foundation of China (Grant Nos. 51432005, 5151101243, 51561145021).

REFERENCES

- (1) Kim, S.; Lim, Y. T.; Soltesz, E. G.; De Grand, A. M.; Lee, J.; Nakayama, A.; Parker, J. A.; Mihaljevic, T.; Laurence, R. G.; Dor, D. M.; Cohn, L. H.; Bawendi, M. G.; Frangioni, J. V. Near-Infrared Fluorescent Type II Quantum Dots for Sentinel Lymph Node Mapping. *Nat. Biotechnol.* **2004**, *22*, 93–97.
- (2) Rauch, T.; Böberl, M.; Tedde, S. F.; Fürst, J.; Kovalenko, M. V.; Hesser, G.; Lemmer, U.; Heiss, Hayden, O. Near-Infrared Imaging with Quantum-Dot-Sensitized Organic Photodiodes. *Nat. Photonics* **2009**, *3*, 332–336.
- (3) Downs, C.; Vandervelde, T. E. Progress in Infrared Photodetectors Since 2000. *Sensors* **2013**, *13*, 5054–5098.
- (4) Blanco, M.; Villarroya, I. NIR Spectroscopy: a Rapid-Response Analytical Tool. *TrAC, Trends Anal. Chem.* **2002**, *21*, 240–250.
- (5) Sargent, E. H. Infrared Quantum Dots. *Adv. Mater.* **2005**, *17*, 515–522.
- (6) Rogalski, A. Recent Progress in Infrared Detector Technologies. *Infrared Phys. Technol.* **2011**, *54*, 136–154.
- (7) Yuang, R.-H.; Chyi, J.-I.; Lin, W.; Tu, Y.-K. High-Speed InGaAs Metal-Semiconductor-Metal Photodetectors with Improved Responsivity and Process Yield. *Opt. Quantum Electron.* **1996**, *28*, 1327–1334.
- (8) Saran, R.; Curry, R. J. Lead Sulphide Nanocrystal Photodetector Technologies. *Nat. Photonics* **2016**, *10*, 81–92.
- (9) Koppens, F. H. L.; Mueller, T.; Avouris, Ph.; Ferrari, A. C.; Vitiello, M. S.; Polini, M. Photodetectors Based on Graphene, Other Two Dimensional Materials and Hybrid Systems. *Nat. Nanotechnol.* **2014**, *9*, 780–793.

- (10) Gong, X.; Tong, M.; Xia, Y.; Cai, W.; Moon, J. S.; Cao, Y.; Yu, G.; Shieh, C.-L.; Nilsson, B.; Heeger, A. J. High-Detectivity Polymer Photodetectors with Spectral Response from 300 to 1450 nm. *Science* **2009**, *325*, 1665–1667.
- (11) Hayden, O.; Agarwal, R.; Lieber, C. M. Nanoscale Avalanche Photodiodes for Highly Sensitive and Spatially Resolved Photon Detection. *Nat. Mater.* **2006**, *5*, 352–356.
- (12) Cao, L.; Park, J.-S.; Fan, P.; Clemens, B.; Brongersma, M. L. Resonant Germanium Nanoantenna Photodetectors. *Nano Lett.* **2010**, *10*, 1229–1233.
- (13) Wang, X.; Cheng, Z.; Xu, K.; Tsang, H. K.; Xu, J.-B. High-Responsivity Graphene/Silicon-Heterostructure Waveguide Photodetectors. *Nat. Photonics* **2013**, *7*, 888–891.
- (14) Almeida, V. R.; Barrios, C. A.; Panepucci, R. R.; Lipson, M. All-Optical Control of Light on a Silicon Chip. *Nature* **2004**, *431*, 1081–1084.
- (15) Wang, Y.; Ding, K.; Sun, B.; Lee, S.-T.; Jie, J. Two-Dimensional Layered Material/Silicon Heterojunctions for Energy and Optoelectronic Applications. *Nano Res.* **2016**, *9*, 72–93.
- (16) Herzinger, C. M.; Johs, B.; McGahan, W. A.; Woollam, J. A.; Paulson, W. Ellipsometric Determination of Optical Constants for Silicon and Thermally Grown Silicon Dioxide via a Multi-Sample, Multi-Wavelength, Multi-Angle Investigation. *J. Appl. Phys.* **1998**, *83*, 3323–3336.
- (17) Wang, Z. L.; Song, J. H. Piezoelectric Nanogenerators Based on Zinc Oxide Nanowire Arrays. *Science* **2006**, *312*, 242–246.
- (18) Wang, Z. L. Progress in Piezotronics and Piezo-Phototronics. *Adv. Mater.* **2012**, *24*, 4632–4646.
- (19) Yang, Q.; Guo, X.; Wang, W.; Zhang, Y.; Xu, S.; Lien, D. H.; Wang, Z. L. Enhancing Sensitivity of a Single ZnO Micro-/Nanowire Photodetector by Piezo-Phototronic Effect. *ACS Nano* **2010**, *4*, 6285–6291.
- (20) Wang, Z.; Yu, R.; Pan, C.; Liu, Y.; Ding, Y.; Wang, Z. L. Piezo-Phototronic UV/Visible Photosensing with Optical-Fiber–Nanowire Hybridized Structures. *Adv. Mater.* **2015**, *27*, 1553–1560.
- (21) Dong, L.; Niu, S.; Pan, C.; Yu, R.; Zhang, Y.; Wang, Z. L. Piezo-Phototronic Effect of CdSe Nanowires. *Adv. Mater.* **2012**, *24*, 5470–5475.
- (22) Wen, X.; Wu, W.; Wang, Z. L. Effective Piezo-Phototronic Enhancement of Solar Cell Performance by Tuning Material Properties. *Nano Energy* **2013**, *2*, 1093–1100.
- (23) Pan, C.; Niu, S.; Ding, Y.; Dong, L.; Yu, R.; Liu, Y.; Zhu, G.; Wang, Z. L. Enhanced Cu₂S/CdS coaxial nanowire solar cells by piezo-phototronic effect. *Nano Lett.* **2012**, *12*, 3302–3307.
- (24) Pan, C.; Dong, L.; Zhu, G.; Niu, S.; Yu, R.; Yang, Q.; Liu, Y.; Wang, Z. L. High-Resolution Electroluminescent Imaging of Pressure Distribution Using a Piezoelectric Nanowire Led Array. *Nat. Photonics* **2013**, *7*, 752–758.
- (25) Yang, Q.; Liu, Y.; Pan, C.; Chen, J.; Wen, X.; Wang, Z. L. Largely Enhanced Efficiency in ZnO Nanowire/P-Polymer Hybridized Inorganic/Organic Ultraviolet Light-Emitting Diode by Piezo-Phototronic Effect. *Nano Lett.* **2013**, *13*, 607–613.
- (26) Pan, C.; Chen, M.; Yu, R.; Yang, Q.; Hu, Y.; Zhang, Y.; Wang, Z. L. Progress in Piezo-Phototronic-Effect-Enhanced Light-Emitting Diodes and Pressure Imaging. *Adv. Mater.* **2016**, *28*, 1535–1552.
- (27) Wong, M.-C.; Chen, L.; Tsang, M.-K.; Zhang, Y.; Hao, J. Magnetic-Induced Luminescence from Flexible Composite Laminates by Coupling Magnetic Field to Piezophotonic Effect. *Adv. Mater.* **2015**, *27*, 4488–4495.
- (28) Chen, L.; Wong, M.-C.; Bai, G.; Jie, W.; Hao, J. White and Green Light Emissions of Flexible Polymer Composites under Electric Field and Multiple Strains. *Nano Energy* **2015**, *14*, 372–381.
- (29) Dou, L.; Yang, Y. M.; You, J.; Hong, Z.; Chang, W.-H.; Li, G.; Yang, Y. Solution-Processed Hybrid Perovskite Photodetectors with High Detectivity. *Nat. Commun.* **2014**, *5*, 5404.
- (30) *Silicon Photodiodes and InGaAs Photodiodes Series*; Hamamatsu Photonics, 2016. <http://www.hamamatsu.com/eu/en/product/category/index.html> (accessed December 2016).
- (31) *Silicon Photodiodes and InGaAs Photodiodes Series*; OSI Optoelectronics, 2016. <http://www.osioptoelectronics.com/standard-products/default.aspx> (accessed December 2016).
- (32) Sun, K.; Jing, Y.; Park, N.; Li, C.; Bando, Y.; Wang, D. Solution Synthesis of Large-Scale, High-Sensitivity ZnO/Si Hierarchical Nanoheterostructure Photodetectors. *J. Am. Chem. Soc.* **2010**, *132*, 15465–15467.
- (33) Manna, S.; Das, S.; Mondal, S. P.; Singha, R.; Ray, S. K. High Efficiency Si/CdS Radial Nanowire Heterojunction Photodetectors Using Etched Si Nanowire Templates. *J. Phys. Chem. C* **2012**, *116*, 7126–7133.
- (34) Akgul, F. A.; Akgul, G.; Gullu, H. H.; Unalan, H. E.; Turan, R. Enhanced Diode Performance in Cadmium Telluride–Silicon Nanowire Heterostructures. *J. Alloys Compd.* **2015**, *644*, 131–139.
- (35) Ni, P.-N.; Shan, C.-X.; Wang, S.-P.; Liu, X.-Y.; Shen, D. Z. Self-Powered Spectrum-Selective Photodetectors Fabricated From n-ZnO/p-NiO Core–Shell Nanowire Arrays. *J. Mater. Chem. C* **2013**, *1*, 4445–4449.
- (36) Sze, S. M. *Physics of Semiconductor-Devices*. *CC/Eng. Technol. Appl. Sci.* **1982**, *27*, 28.
- (37) Yang, Y.; Zhang, H.; Chen, J.; Lee, S.; Hou, T.-C.; Wang, Z. L. Simultaneously Harvesting Mechanical and Chemical Energies by a Hybrid Cell for Self-Powered Biosensors and Personal Electronics. *Energy Environ. Sci.* **2013**, *6*, 1744–1749.
- (38) Bao, R.; Wang, C.; Dong, L.; Shen, C.; Zhao, K.; Pan, C. CdS Nanorods/Organic Hybrid LED Array and the Piezo-Phototronic Effect of the Device for Pressure Mapping. *Nanoscale* **2016**, *8*, 8078–8082.